ENGINEERING

Biofunctionalized conductive polymers enable efficient CO₂ electroreduction

Halime Coskun,[1] Abdalaziz Aljabour,[1,2] Phil De Luna,[3] Dominik Farka,[1] Theresia Greunz,[4] David Stifter,[4] Mahmut Kus,[2] Xueli Zheng,[5] Min Liu,[5] Achim W. Hassel,[6] Wolfgang Schöfberger,[7] Edward H. Sargent,[5] Niyazi Serdar Sariciftci,[1] Philipp Stadler[1]*

Selective electrocatalysts are urgently needed for carbon dioxide (CO₂) reduction to replace fossil fuels with renewable fuels, thereby closing the carbon cycle. To date, noble metals have achieved the best performance in energy yield and faradaic efficiency and have recently reached impressive electrical-to-chemical power conversion efficiencies. However, the scarcity of precious metals makes the search for scalable, metal-free, CO₂ reduction reaction (CO₂RR) catalysts all the more important. We report an all-organic, that is, metal-free, electrocatalyst that achieves impressive performance comparable to that of best-in-class Ag electrocatalysts. We hypothesized that polydopamine—a conjugated polymer whose structure incorporates hydrogen-bonded motifs found in enzymes—could offer the combination of efficient electrical conduction, together with rendered active catalytic sites, and potentially thereby enable CO₂RR. Only by developing a vapor-phase polymerization of polydopamine were we able to combine the needed excellent conductivity with thin film–based processing. We achieve catalytic performance with geometric current densities of 18 mA cm⁻² at 0.21 V overpotential (−0.86 V versus normal hydrogen electrode) for the electrosynthesis of C₁ species (carbon monoxide and formate) with continuous 16-hour operation at >80% faradaic efficiency. Our catalyst exhibits lower overpotentials than state-of-the-art formate-selective metal electrocatalysts (for example, 0.5 V for Ag at 18 mA cm⁻¹). The results confirm the value of exploiting hydrogen-bonded sequences as effective catalytic centers for renewable and cost-efficient industrial CO₂RR applications.

INTRODUCTION

Electrocatalysis of CO₂ has become crucial in generating renewable carbon feedstock and synthetic fuels (1–15). Reductive recycling is essential not only to mitigate anthropogenic climate change but also to use CO₂ as a future nonfossil carbon feedstock. The immense expected throughput of emissions (greater than 30 gigatons of emitted CO₂ per annum) requires superior, inexpensive materials that catalyze the reduction at high energy efficiency. Reducing overpotentials is therefore one important aim to justify the use of renewable energy resources for the energy-intensive production of CO and related hydrocarbons.

Various (noble) metal electrocatalysts are currently available for synthesizing fuels and carbon feedstocks at acceptable energy yields (2, 5–7, 9, 11, 16–19). However, in view of the massive scale-up necessary for industrial use, alternative materials with comparable performance that do not require rare elements with high socioecological impact are urgently needed. One way to eliminate metals that are attracting growing interest is to use renewable and easily recyclable organic electrocatalysts (13, 20–25). This renewable approach is inspired by nature, particularly on the activity of enzymes that catalyze CO₂ reduction at high faradaic and energy efficiency.

Increasingly, principles from enzymology are being incorporated into the design of organic electrocatalysts (21–23). For example, enzyme-related motifs are highly present in polydopamine (PDA), a bio-derived

system based on eumelanin pigments (26). PDA's functional richness (1:1 ratio of hydrogen bond to monomer unit) makes it a catalytic system that offers a significant density of potential hydrogen-bonded active sites (27–40). The catalytic motifs consist of amines and hydroxyl-carbonyl associated via hydrogen bonds (Fig. 1) (41). Within immediate proximity, they are coordinated in inter- or intramolecular conformation and feature a latent nucleophilic sequence that facilitates CO₂ binding.

The role of hydrogen bonding and its nucleophilic character has previously been discussed for electrosynthetic applications, specifically in the context of the nonpolymeric hydrogen-bonded pigments quinacridone and epindolidione (23, 42). They were used in catalytic processes, but at high overpotentials and/or with limited product yields because hydrogen-bonded pigments have an intrinsically low capability for electron transport (23, 42). Consequently, the functional sites dangle and provide poor electrical connection to the carrier electrode showing poor catalytic reactivity.

Here, we first used density functional theory (DFT) to investigate the interactions between CO₂ and the proposed hydrogen-bonded catalytic active sites. We found interactions between hydrogen-bonded sites with latent nucleophilicity and CO₂ were energetically favored.

Inspired by these initial calculations hinting at favorable CO₂ energetics, we sought to overcome the severe limitations of poor electrical transport. We found that conductive PDA is an ideal candidate for developing an effective organic electrocatalytic system when it covers a nonmetallic carrier electrode (carbon fibers): The conductive chain on the inside serves as a wire to supply electrons to the peripheral active sites (Fig. 2). Electrons travel across the entire system as PDA brings together the carrier electrode, conductive body, and catalytic functional groups, which makes it a powerful electrocatalyst.

To achieve conductivity, we established charge doping in the conjugated carrier, which is essential for conductive-conjugated wires that use the effective surface activity. Note that direct doping is hampered

[1]Linz Institute for Organic Solar Cells, Institute of Physical Chemistry, Johannes Kepler University Linz, Altenberger Strasse 69, 4040 Linz, Austria. [2]Department of Chemical Engineering, Selçuk University, 42075 Konya, Turkey. [3]Department of Materials Science and Engineering, University of Toronto, 10 King's College Road, Toronto, Ontario M5S 3G4, Canada. [4]Center for Surface and Nanoanalytics, Johannes Kepler University Linz, 4040 Linz, Austria. [5]Edward S. Rogers Sr. Department of Electrical and Computer Engineering, University of Toronto, Toronto, Ontario M5S 3G4, Canada. [6]Christian Doppler Laboratory for Combinatorial Oxide Chemistry (COMBOX) at Institute for Chemical Technology of Inorganic Materials, Johannes Kepler University Linz, 4040 Linz, Austria. [7]Institute of Organic Chemistry, Johannes Kepler University Linz, 4040 Linz, Austria.
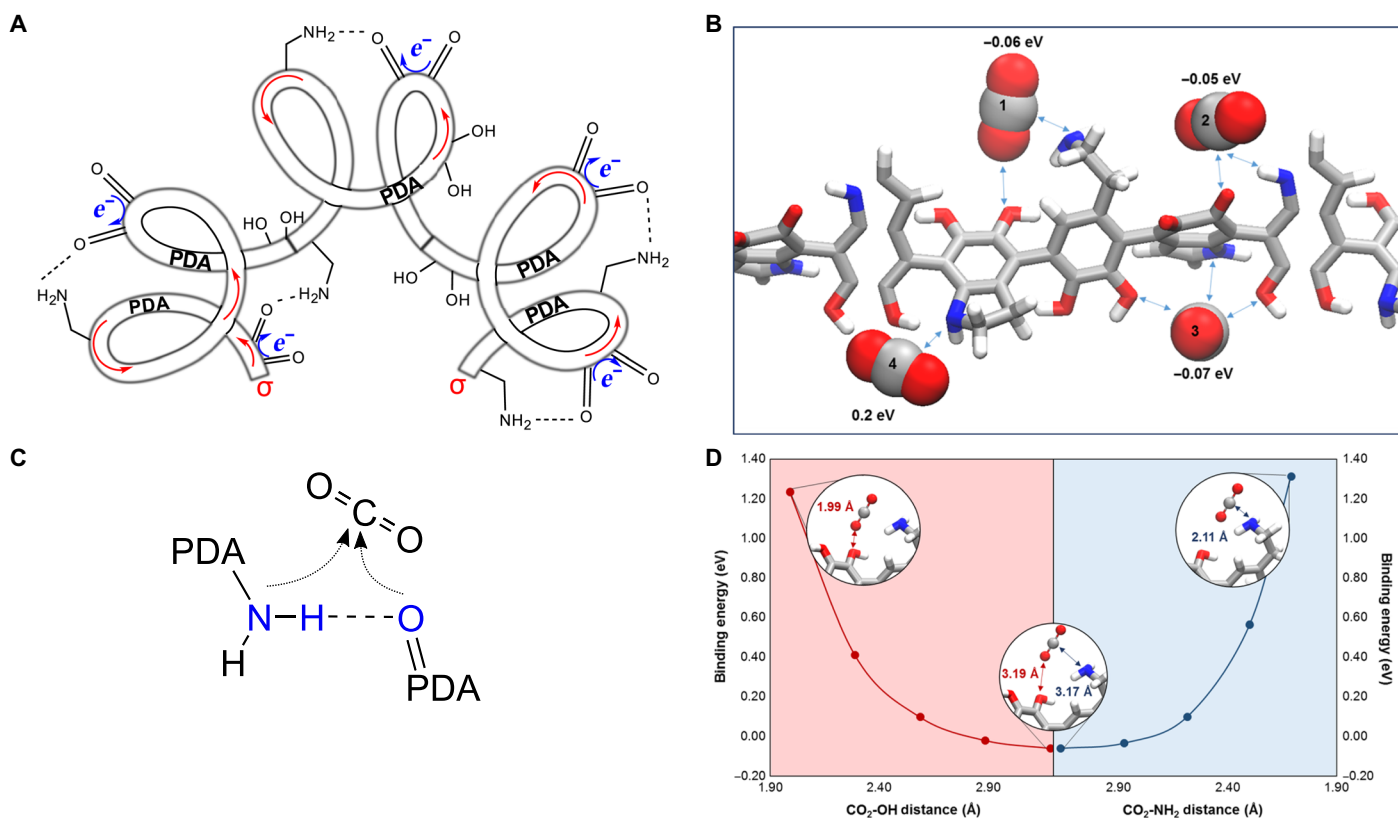*Corresponding author. Email: philipp.stadler@jku.at

Fig. 1. Hydrogen bonds as catalytic motifs for CO_2 reduction. (**A**) PDA electrocatalytic wires consisting of a conjugated-conductive body with functional groups on a carbon-based carrier electrode. (**B** to **D**) The functional groups drive the selective reduction of CO_2, (B) BEs at this site (DFT calculation) for CO_2, (C) two-spot delocalized amine-carbonyl hydrogen–bonded catalytic center on PDA, and (D) BEs shown as functions of the distances between nitrogen and CO_2 (1.99 Å) and oxygen and CO_2 (2.11 Å), indicating the most favorable energy-steric conformation.
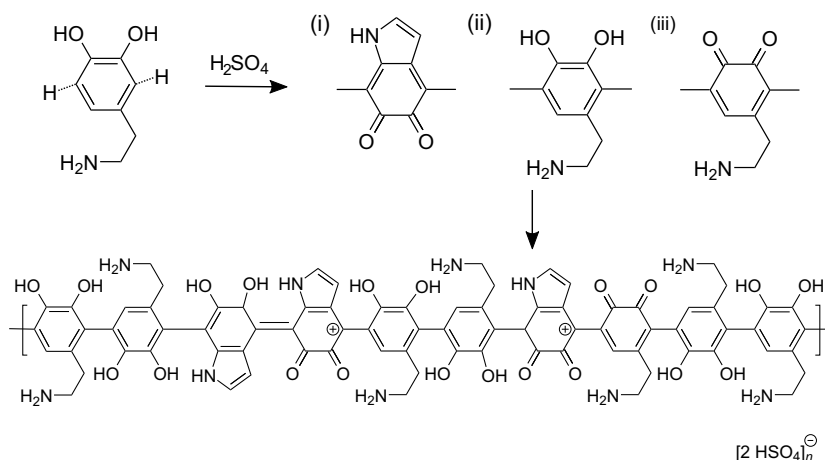

Fig. 2. Synthesis of conductive-catalytic PDA. Reaction of dopamine to conductive PDA by contact with sulfuric acid as oxidant during vapor-phase polymerization involves building blocks such as (i) condensed and oxidized diketoindole, (ii) dopamine, and (iii) oxidized dopamine, yielding the final product with periodically repeating units of conductive PDA.

because hydrogen-bonded frameworks show high inertness (43). To realize this, we introduce a more promising path toward creating conductive bodies: oxidative chemical vapor deposition (oCVD). This method integrates charge doping into the synthesis (polymerization and doping reaction) and creates persistent conductive-conjugated materials; this approach has emerged in the context of established con-

ductive polymers such as PEDOT [poly(3,4-ethylenedioxythiophene)] to provide metal-like conductivities (44, 45). We used the same concept to generate, for the first time, conductive PDA and yielded conductivities of 0.43 S cm^{-1} without compromising catalysis.

Furthermore, the vapor-phase technique used facilitates ease of deposition and effective infiltration of large-surface, sponge-type carbon felt (CF).

This enabled us to demonstrate metal-free electrocatalysis of CO_2 to CO and formate at low overpotentials (210 mV) on par with best-in-class metal-based or transition metal dichalcogenide–based electrocatalysts (3, 4, 4–7, 11, 46). Remarkably, our cathodes exhibited no notable degradation after 16 hours of use.

In particular, the low overpotential paired with significant current densities (approximately 1.4 mA cm^{-2} for CO and 16.9 mA cm^{-2} for formate) and significant turnover demonstrates the power of conductive PDA as a renewable electrocatalyst (the formate turnover frequency is 1.23 hour^{-1}). An investigation of the mechanism responsible for this effectiveness by in situ spectroscopy showed that the hydrogen-bonded sites are ideal for catalysis. Their unexpectedly high performance demonstrates an untapped potential for replacing expensive metals in electrocatalytic applications in a fully renewable scenario.

RESULTS AND DISCUSSION

We began by using DFT to calculate the binding energies (BEs) for hydrogen-bonded sites to CO_2 on PDA periodic structures. We found three favored CO_2 positions (negative BEs between −0.05 and −0.07 eV) proximate to the amine hydroxyl-carbonyl proposed catalytic sites (Fig. 1B) (29). The actual CO_2 distance between nitrogen and oxygen sites varies with local optimum BEs found at 1.99 Å for CO_2-hydroxyl-carbonyl and 2.11 Å for CO_2-amine slightly favoring the former (Fig. 1C). We investigated this initial finding—CO_2 nucleation over carbonyl—by in situ spectral investigations as mentioned later.

Motivated by initial calculations on PDA, we developed a novel conductive synthesis. Conventionally, PDA is derived from aqueous dopamine solutions using oxidative polymerization with ambient O_2 as a reagent. The result is a complex organic system—depending on the exact conditions under which PDA is grown, different structural varieties have been reported (27–30). We transferred the entire established standard synthesis to the gas phase and found that sulfuric acid offers sufficient oxidation power to improve polymerization and doping so that an electrically conducting hydrogen-bonded system can be produced by oCVD (Fig. 2). The resulting polymer forms a polyparaphenylene (PPP) core with periodically repeating patterns of functional groups. As shown earlier, the functionalization is based on variable moieties. We found evidence of (i) indole (condensed secondary amine in an aromatic system with oxidized keto functions), (ii) dopamine, and, in the greatest quantity, (iii) oxidized dopamine (carbonyl function). These dominated other intermediates, which are compounds thereof. The pre-

cise nature of the repeating unit in the polymer was identified by detailed spectral investigations (figs. S12 to S16).

Structural investigations revealed characteristic spectral fingerprints indicative of free charge carriers in the PPP core (Fig. 3A). These are signature infrared-activated vibrations originating from the strong electron-phonon coupling due to doping-induced distortions (47, 48). We also synthesized nonconductive PDA, the spectrum of which lacked these kinds of features. Conductive PDA thin films (typically with thicknesses between 0.5 and 1 μm) exhibit an average (electrical) dc conductivity of 0.43 ± 0.1 S cm^{-1} (Fig. 3B). Additionally, we found distinctive carbonyl oscillations. These spectral features confirm that vapor-based synthesis particularly favors type (iii) moieties (that is, carbonyl over hydroxyl), which play a crucial role in electrocatalysis. We note that the DFT-calculated BEs of CO_2 in between the amine and carbonyl groups were favorable at −0.05 eV.

Initial experiments in electrocatalysis of conductive PDA thin films showed significant dependence of the current on the CO_2 concentration within the electrochemical window of reversibility. We examined the electrochemical parameters thoroughly by defining the applicable window of electrochemical potential [0 to −1800 mV versus normal hydrogen electrode (NHE)] using acetonitrile-water solution [1 volume % water, saturated with N_2 and CO_2 (0.27 M)] (fig. S1).

These results motivated us to demonstrate more effective CO_2 reduction reaction (CO_2RR) by improving the geometric configuration (Fig. 4). To this end, we modified the electrochemical setup and used CF networks as supporting carrier electrodes because they offer a large surface area (of up to 22,000 m^{-1}) and have negligible catalytic activity toward CO_2. Vapor deposition enabled us to effectively infiltrate the felt with conductive PDA to generate a homogeneously covered network for maximum catalytic activity. The corresponding cyclic voltammograms and chronoamperometric scans of the working electrode (WE) as generated show the full performance of our electrocatalyst (Fig. 4A). We observed reductive currents of up to 110 mA cm^{-2} at −1560 mV versus NHE in the presence of CO_2. Insights into the fibrous structure were gained by high-resolution (HR) scanning electron microscopy (SEM) before and after synthesis for 8 hours (Fig. 4B). SEM images reveal a structural roughening of the PDA surface after electrosynthesis. For chronoamperometry, we used an operating potential of −860 mV versus NHE, where we find the best compromise in terms of faradaic efficiency, current density, and overpotential. We performed experimental runs for 16 hours with frequent product cross-checks in parallel (cathode space only). We found H_2, CO, and formate as reaction products. Over
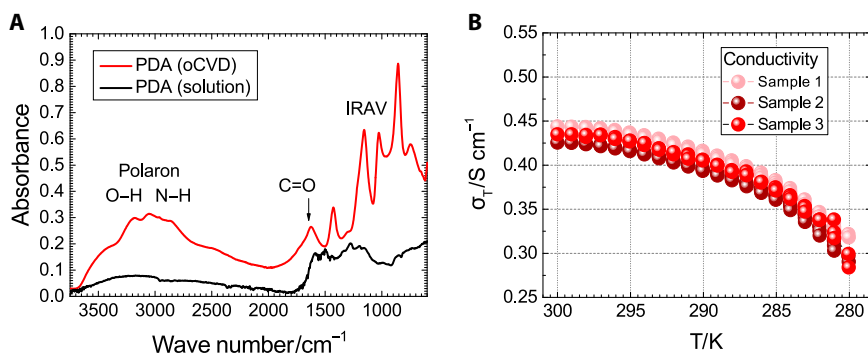
Fig. 3. Fingerprints of free charge carriers in conductive PDA. (**A**) Mid-infrared spectra of nonconductive PDA and conductive PDA, showing fingerprint spectral features for free-carrier generation in the conjugated system, confirmed in particular by signature infrared-activated vibrations (IRAVs). Note the strong carbonyl oscillation, which indicates dominant oxidation of the original hydroxyl groups. (**B**) The dc electrical conductivity (versus T) was as high as 0.43 S cm^{-1} at 300 K in conductive PDA.
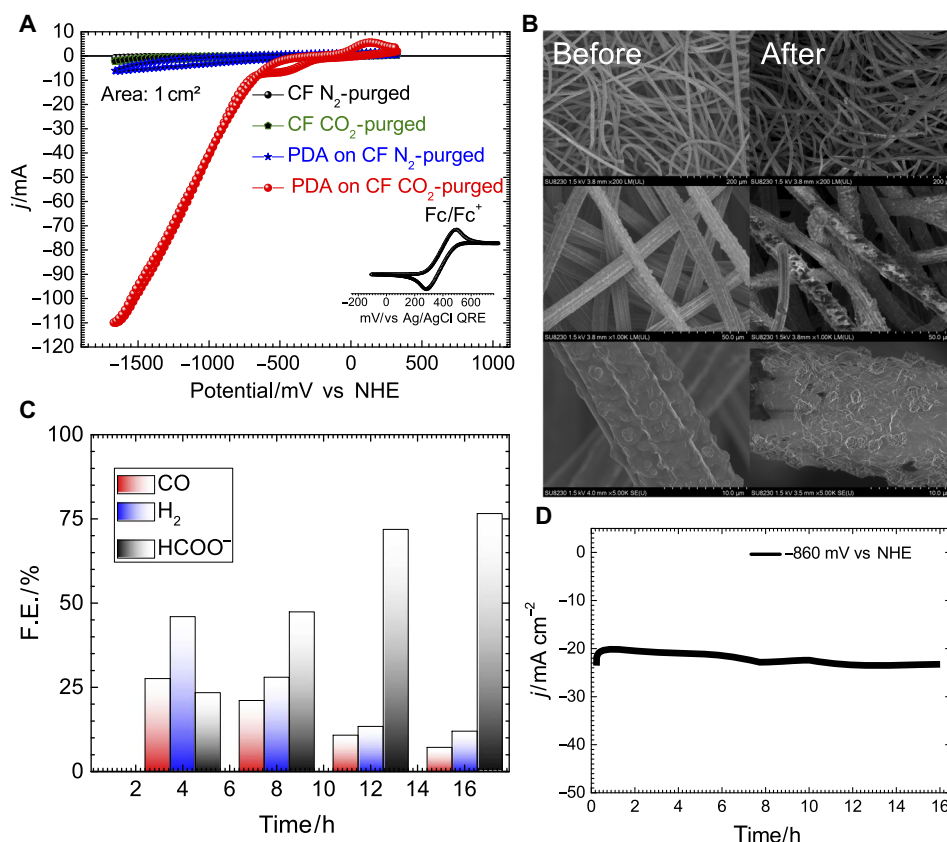
Fig. 4. PDA on CF for the electrocatalysis of CO_2. (**A**) Cyclic voltammogram of conductive PDA on a CF electrode (area, 1 cm²) including control scans. The catalytic activity shows a reductive current in acetonitrile-water purged with CO_2. Fc/Fc⁺, ferrocene/ferrocenium; QRE, quasi-reference electrode. (**B**) SEMs of conductive PDA on CF before and after 8-hour electrocatalysis. (**C**) Faradaic efficiencies (F.E.) of CO, H_2, and formate as functions of time. (**D**) Sixteen-hour chronoamperometric scans (potential, −860 mV versus NHE) showing current stability.

time, we observed a preference for formate, which we attribute to the accumulation of formate and subsequent changes in the local pH (semidiscontinuous electrochemical setting) (Fig. 4C). After 16 hours of operation, the total faradaic efficiency was almost quantitative (95.8%) with 12% for the hydrogen evolution reaction and 83.8% for CO_2RR (7.2% for CO and 76.6% for formate) (Fig. 4D). Note that we used acetonitrile-water (2.65 mole percent H_2O) to avoid precipitation of carbonate and unwanted side reactions in the anode space. The complete electrochemical system released O_2 at the anode and synthesis gas–formate at the cathode. Hence, the operating potential at −860 mV versus NHE corresponded to an overpotential (E^0_{CO,CO_2,CH_3CN} is −650 mV versus NHE) of as little as 210 mV for CO (and formate) (49). This result is on a par with state-of-the-art catalysis and shows the potential of incorporating enzymatic molecular motifs into electrocatalytic processes. Note that the CO_2 origin of electrocatalytic-derived products is confirmed in a separate experiment [marked $^{13}CO_2$ in deuterated solvents by nuclear magnetic resonance (NMR); fig. S4].

Insights into the mechanism and the intermediate processes were gained by in situ spectroelectrochemistry (isSEC) in the fingerprint regime (Fig. 5). This technique enabled us to explore an exact sequence of the electrosynthesis (as a function of the applied potential) and acquire a deeper understanding of why our system favors C_1 species (that is, CO and formate) as dominant products.

The isSEC method allowed us to discriminate between emerging and fading features on the basis of the spectral signs. Although, for in-

stance, the signal of carbonyl-PDA (keto-carbonyl at 1730 cm⁻¹) pointed downward (fading) and that of CO_2 and carbonyl-amide (1650 and 1635 cm⁻¹) pointed upward (emerging). The detailed mechanism in combination with the spectra suggests that CO_2 first attaches to carbonyl-PDA, as can be seen from its subsequent depletion with increasing CO_2 concentration. The final intermediate step involves carbonyl-amide, which forms after attachment and subsequent reduction. This agrees with our calculation, which identified the favored position of the oxygen for initial CO_2 attachment. The subsequent reduction via amide explains the preference for CO and formate and is indicative of the coupling between amino and carbonyl functions via hydrogen bonding.

Active-site enhancement in conductive PDA has the potential to enable industrial electrosynthesis of C_1 carbon feedstocks. Renewable materials are abundant and readily available in natural bio-derived materials. They combine two attractive goals: (i) eliminating expensive (noble) metals and (ii) further reducing overpotentials for superior energy yields in CO_2RR. The latter is a major concern to reduce the amount of energy that must be dissipated in the form of heat at high current densities in industrial-scale electrosynthesis. Furthermore, the approach can be extended to include related enzyme-inspired molecular structures and change the product yield toward higher hydrocarbons or use organic electrosynthesis for hydrogen reactions in fuel cells. Hence, conductive functional materials provide a universal principle for developing efficient electrodes for energy-related electrocatalysis.
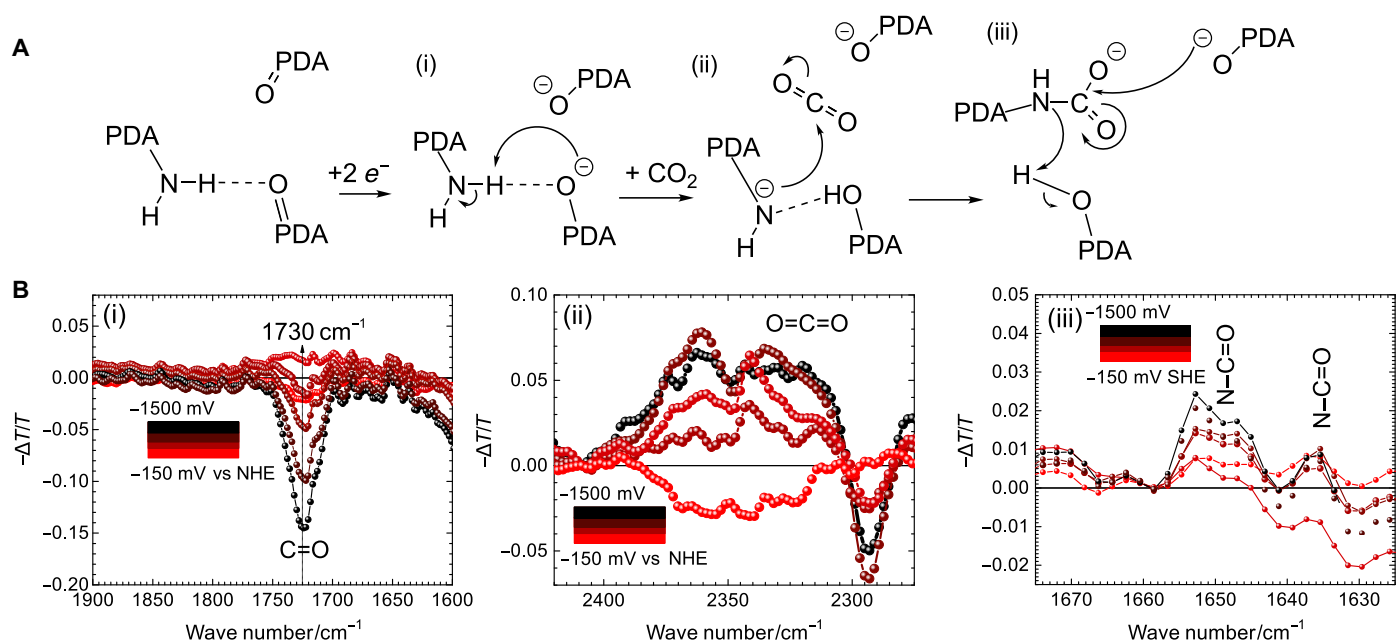
Fig. 5. Electrochemical activation of amine-carbonyl hydrogen bridge to a nucleophilic center. (A) Initial steps driving CO_2RR in conductive PDA: (i) electrochemical activation of the hydrogen-stabilized carbonyl group, (ii) subsequent formation of a nucleophilic center via the adjacent amine, and (iii) attachment to CO_2 creating an amide. **(B)** The in situ Fourier transform infrared (FTIR) differential spectra plot the individual initial steps shown above. The negative signs reflect the depletion of PDA-carbonyl, whereas positive signs correspond to the emergence of new absorptions, that is, CO_2-related vibrations (2350 cm^{-1}) and amide-carbonyl vibrations (1650 and 1635 cm^{-1}). SHE, standard hydrogen electrode.

METHODS

oCVD was conducted on fluorine-doped tin oxide (FTO) glass and CF (10 mm × 10 mm) purchased from the SGL Group–The Carbon Company for electrochemical studies, whereas for low-temperature measurements, sapphire (10 mm × 10 mm × 0.5 mm) purchased from CrysTec Kristalltechnologie with Cr/Au (8 nm/100 nm) electrodes was used. The substrates were cleaned in an ultrasonic bath for 15 min each in acetone, isopropyl alcohol, Hellmanex detergent (Hellma, $70°C$), and deionized water. The metal contacts were deposited by physical vapor deposition through a 4-inch-line contact mask. Before synthesis, dopamine hydrochloride (Sigma-Aldrich) was dried overnight in an oven at $150°C$ in the presence of CaH_2 (95%, Sigma-Aldrich) to remove any residual water. The reaction was carried out in a tube furnace (Carbolite; glass tube length, 45 cm; tube diameter, 2.4 cm; reaction temperature, $300°C$) under nitrogen atmosphere with a carrier gas flow of 3 liter min^{-1}. Sulfuric acid (95 to 97%, J.T.Baker) and sodium sulfate (≥ 99.0%, Sigma-Aldrich) were used as oxidation agents in the synthesis. The reaction time was varied to reach the desired film thickness. A deposition time of 30 min yielded 50-nm films. For electrical characterization, the samples were stored under inert conditions to avoid humidity and were sealed by drop-casting a poly(methyl methacrylate) (PMMA) film on the active area.

The PMMA-covered PDA films on sapphire were contacted using indium solder and loaded to the PPMS DynaCool (Quantum Design). The electrical conductivity was characterized as a function of temperature between 300 and 180 K.

We used FTO and CF as WEs. For this purpose, the FTO substrates were cut into 8-mm × 60-mm pieces and cleaned as described above. PDA was then deposited in the tube furnace at $300°C$ for 1 hour, which resulted in a film thickness of 100 nm. The procedure for CF was the same, except that it was kept in a glove box atmosphere before synthesis

to avoid adsorption of oxygen from the air, and the sponges were pretreated in the tube furnace at $150°C$ for 30 min to prevent any moisture absorption.

To evaluate PDA as an electrocatalyst for CO_2 reduction, we conducted electrochemical studies in a standard three-electrode arrangement in an H-cell configuration. A PDA-coated FTO glass slide and/ or CF was used as a WE, Pt as a counter electrode (CE), and Ag/AgCl as a QRE. All were suspended in a 0.1 M tetrabutylammonium hexafluorophosphate (TBA-PF$_6$) (99.0%, Fluka) in acetonitrile-water (1 volume % H_2O, 0.55 M) as the electrolyte solution. This system offers high CO_2 solubility (approximately 0.27 M) (50). The WE and QRE were placed in one compartment of the H-cell, and the CE in the other (fig. S2). The compartments were connected by a bridge with a membrane (glass frit, porosity no. 2) in between. The Ag/AgCl QRE was calibrated against Fc/Fc$^+$ as an internal reference. All results are given relative to the NHE. The half-wave potential $E_{1/2}$ for Fc/Fc$^+$ was found at $+400$ mV versus QRE (and $+240$ mV versus NHE) (fig. S1D).

The electrochemical setup was characterized by systematic impedance analysis using an IVIUM CompactStat (Netherlands). First, the impedance of the cell (frit-separated H-cell containing acetonitrile + 1 % water, CO_2-saturated, 0.1 M TBA-PF$_6$) was measured using two platinum electrodes. The open circuit potential (OCP) was measured for 30 s and then the electrochemical impedance spectrum was recorded (biased at OCP) in the range from 1 MHz to 1 Hz (perturbation amplitude of 10 mV). The high frequency range was dominated by the resistive behavior of the electrolyte with an absolute impedance of 1.36 kilohm (frequencies, 1 MHz to 1 kHz; equal electrode contribution to impedance due to the full symmetry of the setup). In the next step, the WE was replaced by a CF electrode without catalyst, and the impedance was measured using identical parameters. A value of 857 ohm was obtained (frequencies, 1 MHz to 1 kHz). In the next step, a CF electrode

loaded with PDA catalyst (CF-PDA) was used in a three-electrode arrangement (as for electrosynthesis; reference is Ag/AgCl QRE). The branches were characterized individually resulting in values of 907 ohm (Pt-CE against CF-PDA WE) and 741 ohm (QRE against CF-PDA WE). Note that the amplitude was 1 mV to avoid any deterioration of the QRE. Below 1-kHz phases consistently appeared in the range from −20° to −40°. Finally, the Pt-CE–CF-PDA WE combination was characterized using a three-electrode arrangement, in which the potential at the WE was measured using the reference electrode, and the current was measured between CE and WE. In this way, the actual potential drop in the electrolyte(plus frit including all static and kinetic losses at the CE) is compensated by a correspondingly higher or lower potential at the CE. Eventually, this system only had a low uncompensated electrolyte resistance of maximum 65 ohm (1 MHz to 1 kHz) and 129 ohm down (1 kHz to 1 Hz). This last measurement was performed down to frequencies of 100 mHz, and the phase did not exceed values of −30°. The pH values of the electrolyte solution (0.1 M TBA-PF$_6$ acetonitrile, CO$_2$-saturated) were obtained in the presence of various volume % of water, and for chronoamperometry, using a precision pH meter (Hanna Instruments, model pH 211).

We performed electrochemical and electrosynthesis experiments using a JAISSLE Potentiostat Galvanostat IMP 88 PC. A TRACE Ultra Gas Chromatograph equipped with a thermal conductivity detector was used for analyzing the amount of CO gas produced after electrolysis. All electrochemical experiments were carried out in a glove box atmosphere to avoid moisture absorption. CO$_2$ was introduced to the glove box via a plastic tube from a bottle that contained 99.995% pure CO$_2$, and all chemicals used in the electrochemical experiments were stored only in the glove box. The compartments of the H-cell were purged with N$_2$ and CO$_2$ to achieve complete saturation of the system and prevent possible electrolyte exchange between the compartments that would lead to a change in the CO$_2$ concentration in the environment. The headspace volume was kept constant (20 mL). Before each experiment, the cell was flushed with N$_2$ and then CO$_2$ for 30 min. For the analysis of the insoluble CO gas, 2-ml samples were taken from the headspace by means of a gas-tight syringe and injected manually into the TRACE Ultra Gas Chromatograph (Thermo Fisher Scientific). Helium was used as carrier gas at a flow rate of 20 ml min^{-1}. The thermal conductivity detector was kept at 200°C.

FTIR measurements were carried out with a Bruker Vertex 80 with a range of 8000 to 600 cm^{-1} and a resolution of 4 cm^{-1}. The in situ spectroelectrochemical [attenuated total reflection (ATR)–FTIR] measurements were performed on a Bruker IFS 66/S spectrometer. For the in situ technique, a sealed electrochemical cell (figs. S9 to S11) with Pt as CE, PDA as WE, and Ag/AgCl QRE was mounted in the spectrometer. The system was continuously flushed with 0.1 M TBA-PF$_6$ in acetonitrile. PDA was deposited onto a germanium crystal as a reflection element. During the spectroscopic recording, a cyclic voltammogram was captured between 0 and −2000 mV versus Ag/AgCl.

The chemical surface composition of PDA on Au and CF was evaluated on the basis of x-ray photoelectron spectroscopy (XPS). We used a Theta probe from Thermo Fisher Scientific with an Al Kα (1486.7 eV) source. The charge was compensated by a dual flood gun (1 to 2 eV electrons and Ar$^+$ ions), and the lens mode was set to standard. The energy pass amounted to 200 eV for the survey scan and 50 eV for HR scans, with energy steps of 1 and 0.1 eV, respectively. We used the Avantage v5.32 software package for data analysis. The data fittings were in agreement with the results described in the literature. The elemental concentrations were determined by survey and HR scans (figs.

S12 to S16, PDA on Au). The sulfur concentration was determined on the basis of the S2p and S2s levels. The sulfur concentration was higher than expected [theoretical value, ~2 atomic % (at %); measured values, ~10.7 at % (S2p) and ~8 at % (S2s)].

The N1s level suggested that nitrogen was present in two different chemical environments, predominantly as a primary amine: –R-NH$_2$ (401.8 ± 0.3 eV) and –R-NH-R– (399.9 ± 0.1 eV). The fitting for the C1s spectrum was obtained with three components corresponding to the carbon atoms: CH$_x$ (284.4 ± 0.1 eV), C–O/C–N (286.1 ± 0.2 eV), and C=O (287.7 ± 0.4 eV). The O1s spectrum showed three major contributions: O=C (531.0 ± 0.2 eV), HSO$_4^-$ (531.7 ± 0.2 eV), and O–C (533.0 ± 0.2 eV). HR scans for the elements C, N, O, and S can be seen in figs. S13 to S16. The potential chemical structure of PDA proposed on this basis is shown in Fig. 2.

In addition to the extensive spectroscopic method (XPS and FTIR), we used computational methods for PDA based on DFT (29). This study used a cluster model of four monomer units and Gaussian basis sets for their ab initio simulations. Inspired by this previous study, we began by building a periodic model of a representative system for PDA whereby each monomer type (according to Fig. 2) was accounted for in the polymer structure. We chose this configuration to elucidate the energetics of CO$_2$ binding to each possible monomer unit. The four-unit polymer was placed into a periodic box with dimensions of 17 Å × 15 Å × 15 Å whereby the polymer chain passes through the periodic boundary along the x axis. At least 12 Å of vacuum space along the y and z axes was provided to avoid mirror image effects.

Marked ^{13}CO$_2$ was used for a control experiment to verify that the source of the electrosynthetic product formate was CO$_2$. After chronoamperometric scans, 450 μl of the product solution was used to record ^{13}C NMR on a Bruker Ascend 700 spectrometer equipped with a cryogenically cooled probe (TXI). We use deuterated solvents for the NMR experiments (CD$_3$CN and 1% D$_2$O) (fig. S4).

DFT calculations were performed with the Vienna ab initio simulation package (51). The Perdew-Burke-Ernzerhof generalized gradient approximation exchange correlation functional was used with the projector augmented wave (PAW) method (52, 53). All-electron frozen-core PAW pseudopotentials with Blöchl plane wave basis sets were used with a cutoff energy of 500 eV and a Fermi smearing width of 0.1 eV (54). Long-range van der Waals interactions and dipole corrections were used. Monkhorst-Pack mesh was used for k-point sampling with 6 × 1 × 1 k-points sampled for the structure optimization (55). Structural and unit cell optimizations were performed until the maximum cutoff was less than 0.02 eV per atom with the structures being fully optimized. CO$_2$ was placed in between the amino and carbonyl groups in the hydrogen bond motif of each monomer as a starting point and then fully relaxed (Fig. 1C). The BE for CO$_2$ was calculated as: BE = $E_{PDA+CO2}$ − ($E_{PDA} + E_{CO2}$), where $E_{PDA+CO2}$ is the electronic energy of the system with PDA and the CO$_2$ near the hydrogen bond motif, E_{PDA} is the energy of PDA alone, and E_{CO2} is the energy of gas-phase CO$_2$. Single point calculations were used (CO$_2$ BE as a function of distance) (Fig. 1D) in the two functional sites (oxygen and nitrogen). All images were visualized using the Visual Molecular Dynamics software (56).

SUPPLEMENTARY MATERIALS

REFERENCES AND NOTES

1. M. S. Xie, B. Y. Xia, Y. Li, Y. Yan, Y. Yang, Q. Sun, S. H. Chan, A. Fisher, X. Wang, Amino acid modified copper electrodes for the enhanced selective electroreduction of carbon dioxide towards hydrocarbons. *Energy Environ. Sci.* **9**, 1687–1695 (2016).

2. Z. Wang, G. Yang, Z. Zhang, M. Jin, Y. Yin, Selectivity on etching: Creation of high-energy facets on copper nanocrystals for CO$_2$ electrochemical reduction. *ACS Nano* **10**, 4559–4564 (2016).

3. M. Asadi, K. Kim, C. Liu, A. V. Addepalli, P. Abbasi, P. Yasaei, P. Phillips, A. Behranginia, J. M. Cerrato, R. Haasch, P. Zapol, B. Kumar, R. F. Klie, J. Abiade, L. A. Curtiss, A. Salehi-Khojin, Nanostructured transition metal dichalcogenide electrocatalysts for CO$_2$ reduction in ionic liquid. *Science* **353**, 467–470 (2016).

4. S. Gao, Y. Lin, X. Jiao, Y. Sun, Q. Luo, W. Zhang, D. Li, J. Yang, Y. Xie, Partially oxidized atomic cobalt layers for carbon dioxide electroreduction to liquid fuel. *Nature* **529**, 68–71 (2016).

5. T. S. Safaei, A. Mepham, X. Zheng, Y. Pang, C.-T. Dinh, M. Liu, D. Sinton, S. O. Kelley, E. H. Sargent, High-density nanosharp microstructures enable efficient CO$_2$ electroreduction. *Nano Lett.* **16**, 7224–7228 (2016).

6. M. Liu, Y. Pang, B. Zhang, P. De Luna, O. Voznyy, J. Xu, X. Zheng, C. T. Dinh, F. Fan, C. Cao, F. P. G. de Arquer, T. S. Safaei, A. Mepham, A. Klinkova, E. Kumacheva, T. Filleter, D. Sinton, S. O. Kelley, E. H. Sargent, Enhanced electrocatalytic CO$_2$ reduction via field-induced reagent concentration. *Nature* **537**, 382–386 (2016).

7. H. Mistry, A. S. Varela, C. S. Bonifacio, I. Zegkinoglou, I. Sinev, Y.-W. Choi, K. Kisslinger, E. A. Stach, J. C. Yang, P. Strasser, B. R. Cuenya, Highly selective plasma-activated copper catalysts for carbon dioxide reduction to ethylene. *Nat. Commun.* **7**, 12123 (2016).

8. M. Asadi, B. Kumar, A. Behranginia, B. A. Rosen, A. Baskin, N. Repnin, D. Pisasale, P. Phillips, W. Zhu, R. Haasch, R. F. Klie, P. Král, J. Abiade, A. Salehi-Khojin, Robust carbon dioxide reduction on molybdenum disulphide edges. *Nat. Commun.* **5**, 4470 (2014).

9. Q. Lu, J. Rosen, Y. Zhou, G. S. Hutchings, Y. C. Kimmel, J. G. Chen, F. Jiao, A selective and efficient electrocatalyst for carbon dioxide reduction. *Nat. Commun.* **5**, 3242 (2014).

10. Y. Gong, J. Lin, X. Wang, G. Shi, S. Lei, Z. Lin, X. Zou, G. Ye, R. Vajtai, B. I. Yakobson, H. Terrones, M. Terrones, B. K. Tay, J. Lou, S. T. Pantelides, Z. Liu, W. Zhou, P. M. Ajayan, Vertical and in-plane heterostructures from WS$_2$/MoS$_2$ monolayers. *Nat. Mater.* **13**, 1135–1142 (2014).

11. R. Kas, K. K. Hummadi, R. Kortlever, P. de Wit, A. Milbrat, M. W. J. Luiten-Olieman, N. E. Benes, M. T. M. Koper, G. Mul, Three-dimensional porous hollow fibre copper electrodes for efficient and high-rate electrochemical carbon dioxide reduction. *Nat. Commun.* **7**, 10748 (2016).

12. F. Lei, W. Liu, Y. Sun, J. Xu, K. Liu, L. Liang, T. Yao, B. Pan, S. Wei, Y. Xie, Metallic tin quantum sheets confined in graphene toward high-efficiency carbon dioxide electroreduction. *Nat. Commun.* **7**, 12697 (2016).

13. S. Lin, C. S. Diercks, Y.-B. Zhang, N. Kornienko, E. M. Nichols, Y. Zhao, A. R. Paris, D. Kim, P. Yang, O. M. Yaghi, C. J. Chang, Covalent organic frameworks comprising cobalt porphyrins for catalytic CO$_2$ reduction in water. *Science* **349**, 1208–1213 (2015).

14. J. A. Buss, T. Agapie, Four-electron deoxygenative reductive coupling of carbon monoxide at a single metal site. *Nature* **529**, 72–75 (2015).

15. A. Aljabour, D. H. Apaydin, H. Coskun, F. Ozel, M. Ersoz, P. Stadler, N. S. Sariciftci, M. Kus, Improvement of catalytic activity by nanofibrous CuInS$_2$ for electrochemical CO$_2$ reduction. *ACS Appl. Mater. Interfaces* **8**, 31695–31701 (2016).

16. C. Janáky, D. Hursán, B. Endrődi, W. Chanmanee, D. Roy, D. Liu, N. R. de Tacconi, B. H. Dennis, K. Rajeshwar, Electro- and photoreduction of carbon dioxide: The twain shall meet at copper oxide/copper interfaces. *ACS Energy Lett.* **1**, 332–338 (2016).

17. C. Liu, T. R. Cundari, A. K. Wilson, CO$_2$ reduction on transition metal (Fe, Co, Ni, and Cu) surfaces: In comparison with homogeneous catalysis. *J. Phys. Chem. C* **116**, 5681–5688 (2012).

18. K. P. Kuhl, E. R. Cave, D. N. Abram, T. F. Jaramillo, New insights into the electrochemical reduction of carbon dioxide on metallic copper surfaces. *Energy Environ. Sci.* **5**, 7050 (2012).

19. B. A. Rosen, A. Salehi-Khojin, M. R. Thorson, W. Zhu, D. T. Whipple, P. J. A. Kenis, R. I. Masel, Ionic liquid–mediated selective conversion of CO$_2$ to CO at low overpotentials. *Science* **334**, 643–644 (2011).

20. S. Sultana, P. C. Sahoo, S. Martha, K. Parida, A review of harvesting clean fuels from enzymatic CO$_2$ reduction. *RSC Adv.* **6**, 44170–44194 (2016).

21. N. Khadka, D. R. Dean, D. Smith, B. M. Hoffman, S. Raugei, L. C. Seefeldt, CO$_2$ reduction catalyzed by nitrogenase: Pathways to formate, carbon monoxide, and methane. *Inorg. Chem.* **55**, 8321–8330 (2016).

22. Y.-P. Zhu, Y.-P. Liu, Z.-Y. Yuan, Biochemistry-inspired direct synthesis of nitrogen and phosphorus dual-doped microporous carbon spheres for enhanced electrocatalysis. *Chem. Commun.* **52**, 2118–2121 (2016).

23. M. Jakešová, D. H. Apaydin, M. Sytnyk, K. Oppelt, W. Heiss, N. S. Sariciftci, E. D. Głowacki, Hydrogen-bonded organic semiconductors as stable photoelectrocatalysts for efficient hydrogen peroxide photosynthesis. *Adv. Funct. Mater.* **26**, 5248–5254 (2016).

24. H. A. Hansen, J. B. Varley, A. A. Peterson, J. K. Nørskov, Understanding trends in the electrocatalytic activity of metals and enzymes for CO$_2$ reduction to CO. *J. Phys. Chem. Lett.* **4**, 388–392 (2013).

25. A. M. Appel, J. E. Bercaw, A. B. Bocarsly, H. Dobbek, D. L. DuBois, M. Dupuis, J. G. Ferry, E. Fujita, R. Hille, P. J. A. Kenis, C. A. Kerfeld, R. H. Morris, C. H. F. Peden, A. R. Portis, S. W. Ragsdale, T. B. Rauchfuss, J. N. H. Reek, L. C. Seefeldt, R. K. Thauer, G. L. Waldrop, Frontiers, opportunities, and challenges in biochemical and chemical catalysis of CO$_2$ fixation. *Chem. Rev.* **113**, 6621–6658 (2013).

26. P. Meredith, T. Sarna, The physical and chemical properties of eumelanin. *Pigment Cell Res.* **19**, 572–594 (2006).

27. F. Bernsmann, V. Ball, F. Addiego, A. Ponche, M. Michel, J. J. de Almeida Gracio, V. Toniazzo, D. Ruch, Dopamine−melanin film deposition depends on the used oxidant and buffer solution. *Langmuir* **27**, 2819–2825 (2011).

28. V. Ball, D. Del Frari, V. Toniazzo, D. Ruch, Kinetics of polydopamine film deposition as a function of pH and dopamine concentration: Insights in the polydopamine deposition mechanism. *J. Colloid Interface Sci.* **386**, 366–372 (2012).

29. J. Liebscher, R. Mrówczyński, H. A. Scheidt, C. Filip, N. D. Hădade, R. Turcu, A. Bende, S. Beck, Structure of polydopamine: A never-ending story? *Langmuir* **29**, 10539–10548 (2013).

30. R. A. Zangmeister, T. A. Morris, M. J. Tarlov, Characterization of polydopamine thin films deposited at short times by autoxidation of dopamine. *Langmuir* **29**, 8619–8628 (2013).

31. P. Kanyong, S. Rawlinson, J. Davis, Fabrication and electrochemical characterization of polydopamine redox polymer modified screen-printed carbon electrode for the detection of guanine. *Sens. Actuators B* **233**, 528–534 (2016).

32. J. Y. Lee, T. L. Nguyen, J. H. Park, B.-K. Kim, Electrochemical detection of hydrazine using poly(dopamine)-modified electrodes. *Sensors* **16**, 647 (2016).

33. L. Fu, G. Lai, D. Zhu, B. Jia, F. Malherbe, A. Yu, Advanced catalytic and electrocatalytic performances of polydopamine-functionalized reduced graphene oxide-palladium nanocomposites. *ChemCatChem* **8**, 2975–2980 (2016).

34. C. M. Parnell, B. Chhetri, A. Brandt, F. Watanabe, Z. A. Nima, T. K. Mudalige, A. S. Biris, A. Ghosh, Polydopamine-coated manganese complex/graphene nanocomposite for enhanced electrocatalytic activity towards oxygen reduction. *Sci. Rep.* **6**, 31415 (2016).

35. K. Qu, Y. Zheng, S. Dai, S. Z. Qiao, Graphene oxide-polydopamine derived N, S-codoped carbon nanosheets as superior bifunctional electrocatalysts for oxygen reduction and evolution. *Nano Energy* **19**, 373–381 (2016).

36. H. Peng, C. Liang, Electrochemical determination of hydrazine based on polydopamine-reduced graphene oxide nanocomposite. *Fullerenes Nanotubes Carbon Nanoconstruct.* **25**, 29–33 (2016).

37. S. Palanisamy, B. Thirumalraj, S.-M. Chen, Y.-T. Wang, V. Velusamy, S. Kannan Ramaraj, A facile electrochemical preparation of reduced graphene oxide@polydopamine composite: A novel electrochemical sensing platform for amperometric detection of chlorpromazine. *Sci. Rep.* **6**, 33599 (2016).

38. H. Yang, S. Kang, H. Zou, J. Jin, J. Ma, S. Li, Polydopamine-functionalized multi-walled carbon nanotubes-supported palladium–lead bimetallic alloy nanoparticles as highly efficient and robust catalysts for ethanol oxidation. *RSC Adv.* **6**, 90462–90469 (2016).

39. S. Murali, J.-L. Chang, J.-M. Zen, Bismuth oxide nanoparticles as a nanoscale guide to form a silver–polydopamine hybrid electrocatalyst with enhanced activity and stability for the oxygen reduction reaction. *RSC Adv.* **5**, 4286–4291 (2015).

40. L. Fu, G. Lai, B. Jia, A. Yu, Preparation and electrocatalytic properties of polydopamine functionalized reduced graphene oxide-silver nanocomposites. *Electrocatalysis* **6**, 72–76 (2015).

41. R. R. Knowles, E. N. Jacobsen, Attractive noncovalent interactions in asymmetric catalysis: Links between enzymes and small molecule catalysts. *Proc. Natl. Acad. Sci. U.S.A.* **107**, 20678–20685 (2010).

42. D. H. Apaydin, E. D. Głowacki, E. Portenkirchner, N. S. Sariciftci, Direct electrochemical capture and release of carbon dioxide using an industrial organic pigment: Quinacridone. *Angew. Chem. Int. Ed.* **53**, 6819–6822 (2014).

43. C. Enengl, S. Enengl, M. Havlicek, P. Stadler, E. D. Glowacki, M. C. Scharber, M. White, K. Hingerl, E. Ehrenfreund, H. Neugebauer, N. S. Sariciftci, The role of heteroatoms leading to hydrogen bonds in view of extended chemical stability of organic semiconductors. *Adv. Funct. Mater.* **25**, 6679–6688 (2015).

44. A. Ugur, F. Katmis, M. Li, L. Wu, Y. Zhu, K. K. Varanasi, K. K. Gleason, Low-dimensional conduction mechanisms in highly conductive and transparent conjugated polymers. *Adv. Mater.* **27**, 4604–4610 (2015).

45. S. Lee, K. K. Gleason, Enhanced optical property with tunable band gap of cross-linked PEDOT copolymers via oxidative chemical vapor deposition. *Adv. Funct. Mater.* **25**, 85–93 (2015).

46. P. Abbasi, M. Asadi, C. Liu, S. Sharifi-Asl, B. Sayahpour, A. Behranginia, P. Zapol, R. Shahbazian-Yassar, L. A. Curtiss, A. Salehi-Khojin, Tailoring the edge structure of molybdenum disulfide toward electrocatalytic reduction of carbon dioxide. *ACS Nano* **11**, 453–460 (2017).

47. A. J. Fisher, W. Hayes, D. S. Wallace, Polarons and solitons. *J. Phys. Condens. Matter* **1**, 5567–5593 (1989).

48. C. Cobet, J. Gasiorowski, R. Menon, K. Hingerl, S. Schlager, M. S. White, H. Neugebauer, N. S. Sariciftci, P. Stadler, Influence of molecular designs on polaronic and vibrational transitions in a conjugated push-pull copolymer. *Sci. Rep.* **6**, 35096 (2016).

49. C. Costentin, S. Drouet, M. Robert, J.-M. Savéant, A local proton source enhances CO2 electroreduction to CO by a molecular Fe catalyst. *Science* **338**, 90–94 (2012).

50. Y. Tomita, S. Teruya, O. Koga, Y. Hori, Electrochemical reduction of carbon dioxide at a platinum electrode in acetonitrile-water mixtures. *J. Electrochem. Soc.* **147**, 4164–4167 (2000).

51. J. Hafner, Ab-initio simulations of materials using VASP: Density-functional theory and beyond. *J. Comput. Chem.* **29**, 2044–2078 (2008).

52. P. E. Blöchl, Projector augmented-wave method. *Phys. Rev. B* **50**, 17953–17979 (1994).

53. J. P. Perdew, K. Burke, M. Ernzerhof, Generalized gradient approximation made simple. *Phys. Rev. Lett.* **77**, 3865–3868 (1996).

54. G. Kresse, D. Joubert, From ultrasoft pseudopotentials to the projector augmented-wave method. *Phys. Rev. B* **59**, 1758–1775 (1999).

55. H. J. Monkhorst, J. D. Pack, Special points for Brillouin-zone integrations. *Phys. Rev. B* **13**, 5188–5192 (1976).

56. W. Humphrey, A. Dalke, K. Schulten, VMD: Visual molecular dynamics. *J. Mol. Graph.* **14**, 33–38 (1996).

Citation: H. Coskun, A. Aljabour, P. De Luna, D. Farka, T. Greunz, D. Stifter, M. Kus, X. Zheng, M. Liu, A. W. Hassel, W. Schöfberger, E. H. Sargent, N. S. Sariciftci, P. Stadler, Biofunctionalized conductive polymers enable efficient CO2 electroreduction. *Sci. Adv.* **3**, e1700686 (2017).

Science Advances

Biofunctionalized conductive polymers enable efficient CO$_2$ electroreduction

Halime Coskun, Abdalaziz Aljabour, Phil De Luna, Dominik Farka, Theresia Greunz, David Stifter, Mahmut Kus, Xueli Zheng, Min Liu, Achim W. Hassel, Wolfgang Schöfberger, Edward H. Sargent, Niyazi Serdar Sariciftci and Philipp Stadler

ARTICLE TOOLS	http://advances.sciencemag.org/content/3/8/e1700686
SUPPLEMENTARY MATERIALS	http://advances.sciencemag.org/content/suppl/2017/07/28/3.8.e1700686.DC1
REFERENCES	This article cites 56 articles, 6 of which you can access for free http://advances.sciencemag.org/content/3/8/e1700686#BIBL
PERMISSIONS	http://www.sciencemag.org/help/reprints-and-permissions

Use of this article is subject to the Terms of Service